Stochastic cell-intrinsic stem cell decisions control colony growth in planarians

Tamar Frankovits[1], Prakash Varkey Cherian[1], Yarden Yesharim[1], Simon Dobler[1,2], Omri Wurtzel[1,3]

[1] The School of Neurobiology, Biochemistry & Biophysics, George S. Wise Faculty of Life Sciences, Tel Aviv University, Tel Aviv, Israel

[2] Present address: Interfaculty Institute of Microbiology and Infection Medicine, University of Tübingen, Tübingen, Germany

[3] Sagol School of Neuroscience, Tel Aviv University, Tel Aviv, Israel

* Correspondence: owurtzel@tauex.tau.ac.il

Abstract

Stem cells contribute to organismal homeostasis by balancing division, self-renewal and differentiation. Elucidating the strategies by which stem cells achieve this balance is critical for understanding homeostasis, and for addressing pathogenesis associated with the disruption of this balance (e.g., cancer). Planarians, highly regenerative flatworms, use pluripotent stem cells called neoblasts to maintain and regrow organs. A single neoblast can rescue an entire animal depleted from stem cells and regenerate all cell lineages. How neoblast differentiation and clonal expansion are governed to produce all the required cell types is unclear. Here, we integrated experimental and computational approaches to develop a quantitative model revealing basic principles of clonal growth of individual neoblasts. By experimentally suppressing differentiation to major lineages, we elucidated the interplay between colony growth and lineage decisions. Our findings suggest that neoblasts select their progenitor lineage based on a cell-intrinsic fate distribution. Arresting differentiation into specific lineages disrupts neoblast proliferative capacity without inducing compensatory expression of other lineages. Our analysis of neoblast colonies is consistent with a cell-intrinsic decision model that can operate without memory or communication between neoblasts. This simple cell fate decision process breaks down in homeostasis, likely because of the activity of feedback mechanisms. Our findings uncover essential principles of stem cell regulation in planarians, which are distinct from those observed in many vertebrate models. These mechanisms enable robust production of diverse cell types and facilitate regeneration of missing tissues.

Introduction

Stem cells are crucial for achieving and maintaining homeostasis. Paradoxically, they contribute to an organism's equilibrium through highly dynamic behavior, continuously balancing their population size by regulating rates of self-renewal and differentiation. Understanding the strategies used to accomplish this balance can provide the key to elucidating organismal homeostasis, as well as to modeling pathogenesis associated with disruption to this balance (e.g., cancer) (Passegué et al., 2003; Singh et al., 2011).

Valuable insights into stem cell behavior can be derived from studying systems that rely on principles differing significantly from those characterizing vertebrate stem cells. Neoblasts, the pluripotent stem cells in planarians, function in tissue regeneration and maintenance, providing an intriguing platform in this regard. Neoblasts avoid quiescence, and quickly adapt to changes in organismal requirements by adjusting the quantities and types of cells they produce (González-Estévez et al., 2012; Wagner et al., 2011). These strategies challenge fundamental concepts of vertebrate stem cells. For example, in adult vertebrates, hematopoietic stem cells typically divide slowly, giving rise to rapidly dividing transit amplifying cells forming tissue-specific progenitors (Abkowitz et al., 2000; Becker et al., 2006). These progenitors bear the primary responsibility for maintaining homeostasis. Planarian neoblasts, by contrast, divide rapidly and do not employ transit amplifying cells for progeny production (Pearson, 2022; Raz et al., 2021; van Wolfswinkel et al., 2014). Moreover, neoblasts do not seem to retain substantial memory of the progeny cell types they generate (Raz et al., 2021; van Wolfswinkel et al., 2014). Notably, despite being essentially ageless and immortal, neoblasts do not display cancerous-like states (Van Roten et al., 2018). Therefore, elucidating how neoblasts balance self-renewal and differentiation can contribute to understanding fundamental strategies that facilitate tissue homeostasis and regeneration of lost or damaged tissues (Levin et al., 2019).

Prior modeling of neoblast dynamics in planarians has produced a valuable analytical framework for studying the dynamics of the entire neoblast system (Mangel et al., 2016). However, analyzing isolated neoblasts and their progeny can be instrumental for understanding how decisions are made at a single cell resolution, as well as for deriving physiological parameter values (e.g., corresponding to proliferation and differentiation) that are relevant to the larger system. *In vivo* analysis of individual neoblasts and their progeny is often achieved by applying subtotal irradiation to whole planarians, which results in near-complete neoblast ablation (Wagner et al., 2011). Surviving neoblasts proliferate to form distinct colonies,

allowing analysis of growth dynamics and progeny identity (Lei et al., 2016; Wagner et al., 2012). Though such analysis has been instrumental in uncovering regulators of proliferation and differentiation (Wagner et al., 2012), a quantitative analysis of neoblast colony growth that integrates these principles has yet to be established and experimentally validated.

Several open questions need to be addressed in the development of such a model. For example, it is unclear whether neoblasts select their lineage identity in a synchronous manner or function independently (Bohr et al., 2021; Reddien, 2018). Moreover, as indicated above, it is unclear whether neoblasts maintain memory of their decisions over successive rounds of the cell cycle (Pearson, 2022). In addition, as discussed in what follows, critical knowledge is lacking regarding the ability of neoblasts to switch from producing differentiating lineage to contributing to neoblast colony growth; an understanding of this switch is fundamental for analyzing the overall development of a colony, and for describing new tissue production in regeneration.

Herein, we begin to address these gaps, integrating experimental and computational approaches to analyze neoblast colony growth. Our analysis does not assume communication between neoblasts or memory of cell fate decisions; rather, it explores whether a straightforward stochastic selection of division outcome can adequately describe the growth of a neoblast colony. Based on *in vivo* analysis of neoblast clone growth, neoblast division can result in three potential outcomes (Fig 1) (Lei et al., 2016; Raz et al., 2021): (1) symmetric renewal, which generates two neoblasts; (2) symmetric differentiation, which generates two post-mitotic cells; and (3) asymmetric division, which produces a neoblast and a post-mitotic cell.

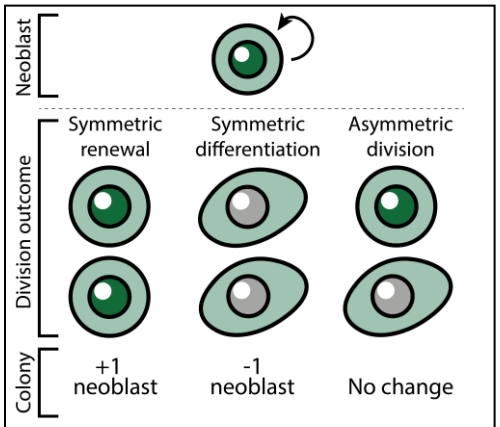

Figure 1. Potential outcomes of neoblast division and the effect on colony size

In what follows, we study and analyze colony growth based on these principles. We derive key parameter values from experimental data and show that these values predict colony growth with high accuracy. Next, in a series of experiments, we seek to uncover whether the core principles that drive neoblast colony growth (as proposed in our model) are further shaped by individual neoblasts' decisions regarding progeny lineage commitment. In particular, many S/G2/M neoblasts express fate-specifying transcription

factors (FSTFs), which direct the differentiation of their progeny into specific lineages (Reddien, 2013; Scimone et al., 2014a; Zeng et al., 2018). Importantly, a neoblast can express different FSTFs in successive rounds of division, which results in production of post-mitotic progenitors of different lineages (Raz et al., 2021; van Wolfswinkel et al., 2014). Thus, the growth potential of the colony is not compromised by FSTF expression. Yet, it remains unclear how the growth of a colony might be affected when expression of a particular FSTF (and thus the corresponding cell lineage) is blocked: for example, does colony growth remain stable, with other lineages being overexpressed to compensate for the blocked lineage? Notably, our experimental perturbation analysis shows that blocking the expression of an FSTF incapacitates a proportion of neoblasts equivalent to the size of the lineage affected. This observation reveals a critical dependency: once a neoblast commits to a specific lineage, it retains this identity until cell division concludes. By contrast, inhibiting FSTFs during homeostasis resulted in an increase in the number of cycling cells, consistent with an activity of feedback mechanisms that regulate cell proliferation in homeostasis (Cheng et al., 2018; Pearson and Sánchez Alvarado, 2010).

Together, our findings imply that simple design principles govern cell fate choices in neoblast colonies, and that accurate prediction of colony growth does not require assumptions of fate-specification memory, or coordination of cell fate choices between neoblasts. Moreover, our findings suggest that all neoblasts in a colony are functionally equivalent (i.e., able to self-renew and to divide to all cell types), and elucidate the contribution of decisions in individual planarian stem cells to achieving systemic homeostasis.

Results

Analysis of neoblast colony growth

Following subtotal irradiation, a surviving neoblast may proliferate to form a colony (Fig 2A). The growing colony is the exclusive source of new cells (Wagner et al., 2012, 2011). We used an exponential growth equation to estimate the change in colony size over time of a successfully established colony by a surviving neoblast (Eq 1). The function incorporates three parameters to estimate colony growth: (1) average cell cycle length (τ); (2) symmetric renewal probability (p), where symmetric renewal rate per hour is $p' = p/\tau$; and (3) symmetric differentiation or neoblast elimination probability (q), where symmetric differentiation or neoblast elimination rate per hour is $q' = q/\tau$. Asymmetric divisions do not alter neoblast count (Fig 1).

$$\frac{dN}{dt} = p'N - q'N = \frac{(p-q)N}{\tau} \qquad [1]$$

We used the solution to the equation, and included the initial colony size (N_0), to predict colony sizes (Eq 2) using a range of parameter values and evaluated the model predictions (Fig 2B; Fig S1) with our own and published data (Raz et al., 2021; Wagner et al., 2012).

$$N(t) = N_0 e^{\frac{(p-q)t}{\tau}} \quad [2]$$

The plots in Figure 2B show how varying the value of growth parameters is predicted to affect colony size. The average cell division time (τ) has the most substantial impact on colony growth. For example, a simulated colony with a fast (16 hours) cell cycle (with p and q set at 0.5 and 0, respectively) had a neoblast count approximately ten times larger than that reported in literature (Lei et al., 2016; Raz et al., 2021; Wagner et al., 2012, 2011; Zeng et al., 2018). To determine the average cell cycle time (τ), we re-analyzed available colony growth data that had previously been experimentally obtained using bromodeoxyuridine (BrdU) metabolic labeling (Lei et al., 2016). In those experiments, BrdU was incorporated into DNA during both symmetric and asymmetric divisions using a pulse (4 hours) significantly shorter than the cell cycle time, followed by a chase of up to 72 hours (Fig 2C). We predicted that the $BrdU^+$ cell number would grow linearly until the entire population doubled. Then, completion of successive cell divisions would lead to exponential growth in $BrdU^+$ cell number. Indeed, the colony growth was initially linear (Pearson r = 0.997), and using linear regression, we estimated that the colony doubling time, and hence the average cell cycle length, was 29.7 hours (Fig 2C).

The symmetric renewal probability (p) is a vital factor in colony growth, and even slight variations in p have large cumulative effects (Fig 2B). We experimentally determined the symmetric renewal probability by subjecting planarians to subtotal irradiation (1750 rad; Methods) and identifying neoblasts via fluorescence *in situ* hybridization (FISH) with the *smedwi-1* marker (Reddien et al., 2005b), a pan-neoblast marker. We imaged pairs of adjacent *smedwi-1*$^+$ cells in the colony, and classified the *smedwi-1*$^+$ cell pairs based on their *smedwi-1* expression levels: high-level pairs indicated symmetric renewal, while pairs with one high and one low *smedwi-1*$^+$ cell categorized as asymmetric division (Fig 2D). By analyzing 40 dividing pairs we estimated that 50% of divisions that produce at least one neoblast are symmetric renewal divisions, in agreement with previous findings (Lei et al., 2016; Raz et al., 2021).

The value of q, representing symmetric differentiation and neoblast loss probability (Raz et al., 2021), also plays a role in colony dynamics (Fig 2E, S1B). Yet the value of this parameter is more difficult to estimate

experimentally (e.g., naïve measurement of cell death using TUNEL in irradiated planarians would be insufficient, because cell death is not limited to neoblasts). We analyzed the effect of different neoblast elimination probabilities on colony size (Fig 2E; Fig S1B-E), and compared the estimates of the analysis with colony size in our experimental data and by extracting colony size measurements from published literature (Fig 2E-F; Methods) (Raz et al., 2021; Wagner et al., 2012, 2011). Considering an average cell cycle length of 29.7 hours, we calculated the value of q using the following approach: the probabilities of all cell division outcomes must sum to 1. Our experimental data showed that symmetric renewal (p) and asymmetric division (a) occur at equal rates (i.e., $p = a$). By fitting these parameters to the experimental data, we determined that the difference between the probabilities of symmetric renewal and symmetric differentiation (i.e., $p - q$) was = 0.345 (Fig 2E, S1D-E). Therefore, with these criteria, we estimated the probabilities of cell division outcomes in the colony as $p = 0.45$, $a = 0.45$, and $q = 0.1$ (Fig 2G; Methods). *In vivo*, we observed a large variation in the size of colonies at each time point (Fig 2F). This could be a consequence of an altered delay between irradiation and the onset of colony growth, or from a stochastic decision to undergo symmetrical or asymmetrical division in the early colony. Despite this variability, the observed exponential growth suggested a steady proliferation rate once the colony founding neoblast recovered at day four (Fig 2E, S1A).

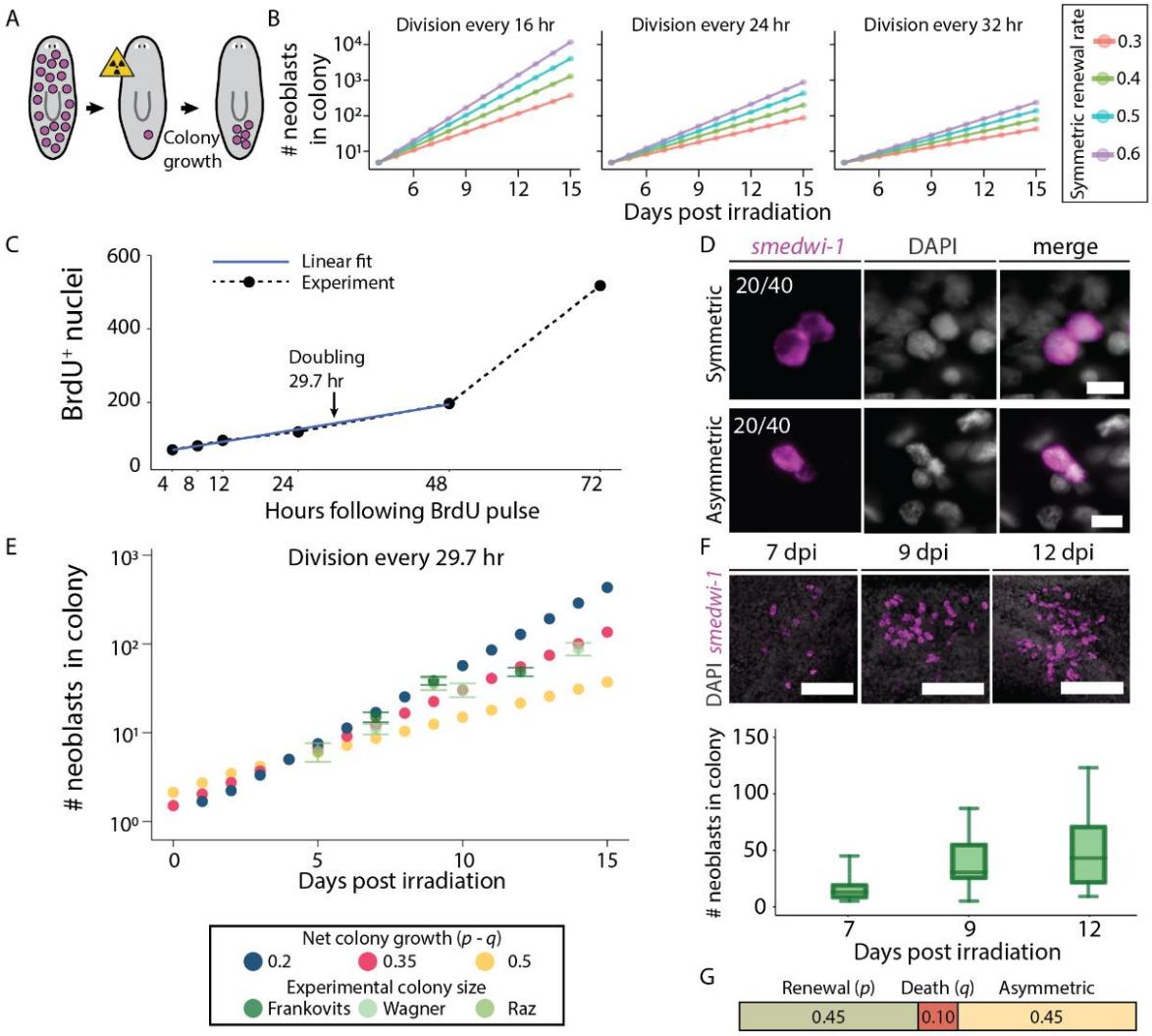

Figure 2. Parameters determining neoblast colony size. (A) Outline of colony growth following subtotal irradiation. Planarians are irradiated to eliminate all neoblasts (purple dots) except for a single survivor. The surviving neoblast forms a proliferating neoblast colony. (B) The impact of average cell cycle length (τ) and probability of symmetric renewal division (*p*) on colony size is shown (*q* was set to 0). (C) Re-analysis of BrdU incorporation time series (Lei et al., 2016) in expanding planarian colonies was used for determining the average cell cycle length (Methods). Linear regression (blue line; y = 59.77 + 2.81 * t; Pearson r = 0.997) was used to identify the doubling time of the colony, and was determined as 29.7 hours (black arrow). (D) The fraction of symmetric renewal divisions was estimated by examining neoblast pairs in colonies at 7 dpi (Methods). Scale = 10 µm. (E) The impact of symmetric differentiation or neoblast elimination (*q*) on colony size was tested, assuming a 29.7 hour long cell cycle. Experimental data of colony sizes at different time points were overlaid to determine the value of biologically relevant parameter. Frankovits, data collected here; Wagner, reanalysis (Wagner et al., 2012); Raz, reanalysis (Raz et al., 2021). Error bars show the standard error. (F) Shown are neoblast colonies at three time points following subtotal irradiation. Representative images (z-projection) are shown (top), and neoblast counting of different colonies is shown (bottom; box indicates interquartile range (IQR); whiskers show range; horizontal bar indicates median). Scale = 100 µm. (G) Summary of the estimated probabilities of divisions leading to symmetric renewal, symmetric differentiation or elimination, and asymmetric divisions.

188 **Inhibition of lineage differentiation reduces neoblast colony size**

189 Regulating growth and homeostasis requires balancing self-renewal and progeny production. To better
190 understand how neoblasts maintain this balance, we focused on the interplay between the overall growth
191 of the colony and the ability of individual neoblasts to express FSTFs, which are required for specific
192 progeny production (Scimone et al., 2014a). More specifically, we investigated how inhibiting
193 differentiation into specific lineages, by suppressing FSTF expression, influences colony size. Considering
194 the linear correlation between post-mitotic progeny production and neoblast number (van Wolfswinkel
195 et al., 2014; Wagner et al., 2012), we hypothesized three potential outcomes (Fig 3A) and their probable
196 effects on symmetric renewal (*p*) and symmetric differentiation or elimination (*q*): (1) Unchanged: *p* and
197 *q* remain balanced, resulting in no change in colony size. This outcome would suggest that the balance of
198 self-renewal and progeny generation is preserved through compensatory production of alternative cell
199 types when differentiation to a specific lineage is suppressed. (2) Larger: An increase in *p*, leading to larger
200 colonies, possibly due to fewer asymmetric divisions in the blocked lineage. (3) Smaller: An increase in *q*,
201 leading to smaller colonies, possibly because neoblasts committed to the blocked lineage have become
202 dysfunctional. We used published frequencies of three major lineages (epidermis, intestine, and *foxF-1*$^{+}$
203 neoblasts) to estimate the size of the colony in each of the described scenarios (Fig 3A) (Raz et al., 2021;
204 Scimone et al., 2014a, 2018; van Wolfswinkel et al., 2014). Theoretically, inhibiting a predominant
205 lineage, such as the epidermal lineage (28%), may significantly affect colony size, which could be observed
206 experimentally, whereas changes in colony size following inhibition of smaller lineages could be difficult
207 to distinguish within the experimental time scale.
208
209 On the basis of this assumption, we inhibited differentiation into the epidermal lineage after subtotally
210 irradiating planarians. Following a four-day recovery after subtotal irradiation, we suppressed the FSTF
211 *zfp-1*, which is critical for production of differentiating epidermal progenitors (Fig S2) (Cheng et al., 2018;
212 Tu et al., 2015; van Wolfswinkel et al., 2014; Wagner et al., 2011), but does not impact directly other
213 lineages (van Wolfswinkel et al., 2014). Then, we evaluated neoblast colony sizes in *zfp-1*-suppressed (*zfp-*
214 *1* (RNAi)) planarians at three time points (7, 9, and 12 days post-irradiation; dpi), and compared them with
215 control colony sizes (Fig 3B, Methods). Initially (7 dpi), colony sizes were similar. However, at 9 dpi, *zfp-1*
216 (RNAi) colonies were significantly smaller than in controls. Moreover, unlike in controls, *zfp-1* (RNAi)
217 colonies showed no additional growth, on average, during the period between 9 dpi and 12 dpi, though
218 there was a slight increase in the median colony size (Fig 3B).
219

220 Our basic assumption was that reduction in colony size (vs. control) following *zfp-1* inhibition would
221 indicate an increase in symmetric differentiation or elimination (*q*). However, an alternative possibility is
222 that *zfp-1* inhibition causes mitotic arrest in neoblasts—which would prevent proliferation but would not
223 necessarily result in cell death. We tested whether *zfp-1* (RNAi) colonies had fewer cycling neoblasts. We
224 detected neoblasts in mitosis using immunofluorescence (IF) with an anti-H3P-antibody (Fig 3C; Methods).
225 We found that control colonies did not significantly differ from *zfp-1* (RNAi) colonies in the number of
226 $H3P^+$ cells, either in absolute numbers or normalized to average neoblast counts in colonies (Methods).
227 This result suggested that FSTF inhibition did not cause a general mitotic arrest. Further analysis with
228 2'-Deoxy-2'-fluoro-5-ethynyluridine (EdU) labeling (Fig 3D; Methods) showed a substantial decrease in
229 EdU^+ nuclei in *zfp-1* (RNAi) animals (vs. controls), indicating reduced new cell production. However,
230 normalizing EdU^+ nuclei to average colony size (Fig 3D; Methods) revealed a comparable proportion of
231 cells entering S-phase. Given the unchanged ratios of cycling and mitotic cells, we can conclude that the
232 diminished colony size following *zfp-1* suppression is indeed likely to result either from increased
233 symmetric differentiation or neoblast elimination (*q*). We further suggest that neoblast elimination is a
234 more plausible explanation than increased symmetric differentiation: If *zfp-1* suppression were to lead to
235 increased symmetric differentiation, we would expect to observe a noticeable decline in the number of
236 neoblasts within colonies, while proliferation rates remained stable. Yet, the non-significant difference in
237 EdU-labeling (Fig 3D) between *zfp-1* (RNAi) and control colonies suggested that inhibition of the FSTF
238 *zfp-1* likely led to increased neoblast elimination.

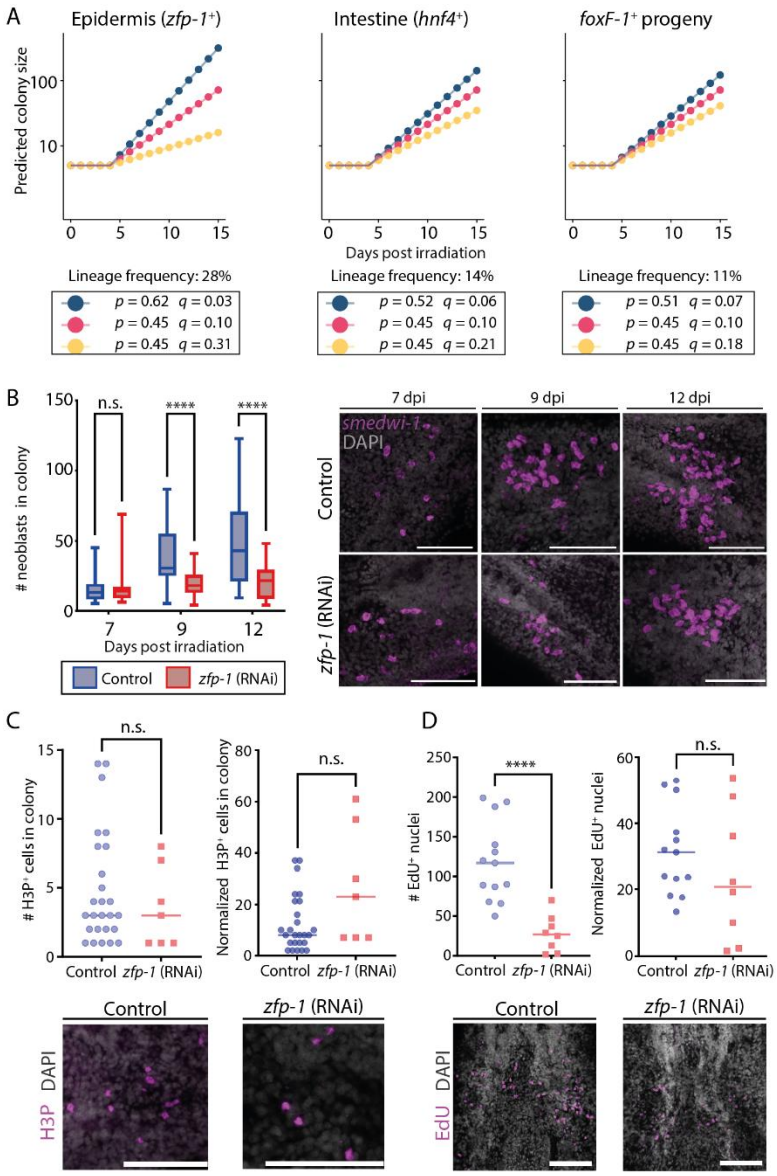

Figure 3. Reduced neoblast colony size following lineage specification block. (A) Models for lineage growth. Potential outcomes of lineage inhibitions were assessed by altering the colony growth and degradation parameters. Applying known lineage frequencies (Raz et al., 2021) to the models indicated that inhibiting production of a major lineage could dramatically impact colony size (left, epidermis). By contrast, inhibition of smaller lineages (middle, right) might have a smaller impact, which would be difficult to detect (Blue: increase in symmetric renewal; red: unchanged renewal and degradation; yellow: increase neoblast degradation). Growth was calculated using the following values: $N_0 = 5$, $\tau = 29.7$ hr, and growth lag time of 5 days (Raz et al., 2021; Wagner et al., 2012). (B) Shown are counts (left) of neoblasts in colonies at three time points following irradiation, which was followed by inhibition of *zfp-1* or control by RNAi. Lineage inhibition resulted in a highly significant decrease in colony size at later time points (box indicates IQR, whiskers show range, bar indicates the median). Number of control colonies analyzed at 7 dpi n = 28; at 9 dpi n = 30; at 12 dpi n = 30; Number of *zfp-1* (RNAi) colonies analyzed at 7 dpi n = 15; at 9 dpi n = 30; at 12 dpi n = 30. Representative colonies (z-projection) are shown (right). (C) Comparison of absolute (top-left) or normalized (top-right) H3P⁺ cell number in *zfp-1* (RNAi) and control colonies at 12 dpi showed a non-significant difference

(Methods). Representative H3P labeling images are shown (Bottom). Importantly, the number of detectable H3P$^+$ cells was small. (D) Comparison of (top-left) EdU$^+$ nuclei in *zfp-1* (RNAi) and control colonies at 12 dpi showed a significant reduction, contributing to the smaller colony size. Comparison of normalized EdU$^+$ nuclei numbers (top-right) showed a non-significant difference, indicating that a similar proportion of neoblasts in the colony were cycling (Methods). Representative EdU labeling images (z-projection) are shown (Bottom). Statistical significance was assessed using Mann-Whitney two-tailed test (Methods). n.s., not significant, ** *P* < 0.0001. Scale = 100 µm.**

Specialized neoblasts are produced in *zfp-1* (RNAi) colonies

Building upon our findings regarding lineage-specific inhibition effects, we next investigated how RNAi of *zfp-1* affected the prevalence of other specialized neoblasts in colonies. We hypothesized that if neoblast elimination was the primary effect of *zfp-1* inhibition, we would observe an absolute decrease in specialized neoblasts of other lineages (e.g., intestine), but not necessarily a relative decrease. We used subtotal irradiation, and following recovery we inhibited *zfp-1*. Then, we counted specialized neoblasts expressing intestine lineage markers (Scimone et al., 2014a; Wagner et al., 2011) , and *tgs-1* (Raz et al., 2021; Zeng et al., 2018), which is suggested to label neural progenitors (Fig 4A-B; Methods). Both control and *zfp-1* (RNAi) colonies contained specialized neoblasts. Notably, a decrease in intestine specialized neoblasts was detectable, aligned with the reduced colony size (Fig 4A). No change was observed in *tgs-1*$^+$ cells, likely due to the low number of *tgs-1*$^+$ cells detected in the colony (2 cells on average) (Fig 4B). Together, these results suggested that specialized neoblasts were produced in *zfp-1* (RNAi) colonies, but that production of other (non-suppressed) lineages did not increase. This indicated that neoblast elimination predominantly accounted for the reduction in colony size following suppression of the epidermal lineage, without compensation by overproduction of other lineages.

To further analyze the impact of *zfp-1* inhibition on colony growth, we examined the numbers of neoblasts in 64 control colonies and in 53 *zfp-1* (RNAi) colonies, at 12 dpi (Fig 4C-D). The proportion of colonies containing five or more neoblasts was greater in the control group (75%) than in the *zfp-1* (RNAi) group (45%; Fisher's exact test two-tailed $P = 2.4\text{x}10^{-5}$). Importantly, more *zfp-1* (RNAi) animals failed to develop colonies compared to controls (55% and 25%, *zfp-1* (RNAi) and control colonies, respectively). This might have resulted from the stochastic selection of a *zfp-1* identity by the neoblasts that initially established the colony, and which led to their further dysfunction, and was therefore detrimental to the development of the colony.

281 **Simulation of colony growth following *zfp-1* inhibition**

282 We developed a simulation to recapitulate the observed reduction in colony growth following *zfp*-1
283 inhibition. Our simulation methodology was designed to mimic real-world neoblast dynamics under *zfp-1*
284 inhibition in a colony, using empirically derived probabilities for each cell cycle outcome. First, we
285 randomly sampled initial colony sizes from the set counted at 7 dpi (Fig 3B). In every simulation cycle,
286 each neoblast fate was selected based on the probabilities of cell cycle outcomes identified above, derived
287 from empirical data (symmetric renewal, asymmetric division, symmetric differentiation or elimination;
288 Fig 2G). The change in colony size was calculated over approximately six cell cycles. We conducted 100
289 iterations per simulation and compared the results with experimental data (Fig 4E; Methods). The
290 simulated colony sizes closely matched the experimental observations. When simulating *zfp-1* (RNAi)
291 colony growth by increasing the symmetric differentiation or elimination probability (q) by the known
292 proportion of *zfp-1*$^{+}$ neoblasts, the model recapitulated the experimental findings (Fig 4E-F). Notably,
293 many simulated *zfp-1* (RNAi) colonies failed to grow, often because of initial sampling of a state of
294 symmetric differentiation or elimination, prohibiting further development of the colony (Fig 4F).

295 The agreement of these simulations with the experimental results is aligned with a model where neoblasts
296 independently select their cell cycle outcome based on a replication outcome distribution without
297 maintaining any memory of previous replication outcomes. Moreover, inhibition of a gene required for
298 neoblast differentiation (e.g., FSTF) impedes the contribution of neoblasts that randomly selected this
299 identity from any further contribution to colony growth across the timescale of the simulation.

300 **Combined suppression of low-frequency lineages affects neoblast colony formation**

301 Our model and simulations indicate that inhibition of smaller lineages will not result in detectably smaller
302 colonies (Fig S3A-C). We tested this model prediction by comparing colonies produced following
303 suppression of intestine lineage progenitors (Forsthoefel et al., 2012; van Wolfswinkel et al., 2014;
304 Wagner et al., 2011), which account for 14% of the produced progenitors (Raz et al., 2021). Indeed, highly
305 efficient inhibition of the intestine lineage by RNAi (Fig S3D), did not result in reduced colony size or colony
306 production, in agreement with our model (Fig 4G-H, S3A). This result corroborated the model's predictions
307 regarding lower-frequency lineages (Fig 3A): the potential increase in q following suppression of
308 differentiation to a lower-frequency lineage had undetectable effect on colony size. Furthermore, the
309 model predicts that inhibition of several lineages, which collectively amount to a larger fraction of

310 produced progenitors, may generate a detectable difference in colony size and successful colony
311 establishment. We co-suppressed the production of intestine lineage together with *foxF-1*$^{+}$ progenitors,
312 which together amount to ~25% of the progenitors (Raz et al., 2021), following subtotal irradiation (Fig
313 4I-J). The co-inhibition of the two lineages resulted in a highly significant decrease in colony size (Fig 4I)
314 and a significant increase in the failure to establish colonies (Fig 4J; 12/23; 52%), compared to their
315 controls (4/18; 22%; Fisher's exact test two-tailed $P = 1.8\text{x}10^{-5}$).

316 These results reinforce the hypothesis that FSTF inhibition reduces colony growth (vs. control), primarily
317 through increased neoblast elimination, without compensatory increases in other lineages. The results
318 also suggest that a neoblast that has selected an identity, but that cannot complete proliferation and
319 differentiation, will not be able to adopt any other identity in this experimental timescale. Based on these
320 conclusions, we propose a semi-stochastic model for selecting the outcome of neoblast division, assuming
321 no memory or coordination between cells, that is sufficient for describing neoblast colony growth.

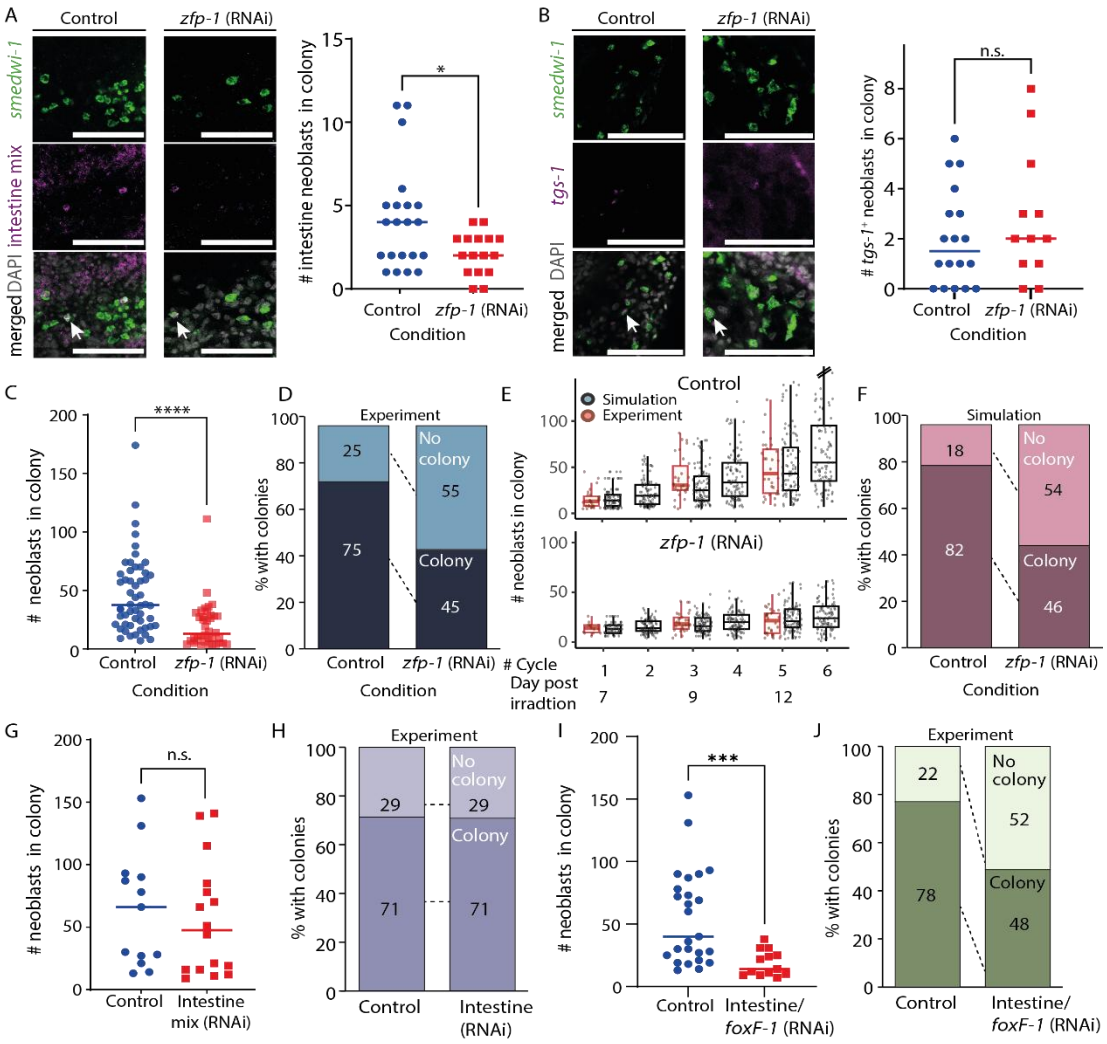

Figure 4. Simulation of neoblast colony growth following lineage block. (A-B) Neoblasts expressing lineage gene expression markers were detected using FISH (intestine mix: *hnf-4, gata4/5/6,* and *nkx2.2*; *tgs-1*), and were counted in colonies of control and *zfp-1* (RNAi) animals at 12 dpi (Methods). Left panels show confocal images of representative colonies (Methods); quantification of the experiment is shown on the right. Scale= 100 µm. (C) Comparison of colony size in control and in *zfp-1* (RNAi) animals 12 dpi showed a highly significant reduction in the size of *zfp-1* (RNAi) colonies (Mann-Whitney two-tailed test, ** *P* < 0.0001). Data is also shown in Fig 3B. (D) Summary of colony production in control and *zfp-1* (RNAi) animals based on analysis of 64 and 53 control and *zfp-1* (RNAi) colonies, respectively, at 12 dpi. Developed: ≥ 5 neoblasts detected; No colony < 5 neoblasts detected. (E) Simulation of colony growth in control and *zfp-1* (RNAi) animals, bottom and top, respectively (Methods). Shown are multiple iterations (black dots; n = 100 for each condition) of colony size simulation starting at 7 dpi. Experimental data quantifying colony sizes are shown (red dots) next to the corresponding simulation cycle. Box indicates the IQR; whiskers indicate ±1.5 x IQR; values out of the whisker range (outliers) were removed for clarity. (F) Summary of colony production in simulated control and *zfp-1* (RNAi) animals based on experimentally determined lineage frequencies, and assuming no memory in division outcome decision. Developed colony: ≥ 5 neoblasts in the simulation on day 12. (G) Neoblasts were counted in colonies at 12 dpi following the inhibition of intestine progenitors by combined RNAi treatment (*hnf-4*,**

337 ***gata4/5/6*, *nkx2.2*). Lineage inhibition did not affect colony size (Mann-Whitney two-tailed test, *P* = 0.404; n=13 and 16, control**
338 **and RNAi animals, respectively). (H) Suppression of intestine lineage did not affect the likelihood of producing colonies (n = 21**
339 **and 24, control and RNAi animals, respectively). (I-J) Combined suppression of *foxF-1* (Scimone et al., 2018) and intestine**
340 **lineage production resulted in smaller colonies (Mann-Whitney two-tailed test, *P* = $3x10^{-4}$) and a significant reduction in the**
341 **likelihood of producing colonies (Fisher's exact test two tailed *P* = $1.8x10^{-5}$).**

342 **Inhibition of *zfp-1* does not induce overexpression of other lineages in homeostasis**

343 Clonal analysis is a powerful approach for studying neoblast proliferation and progeny production.
344 However, stem cell behavior in homeostasis may differ from that observed in clonal growth. For example,
345 unlike in clonal expansion, the stem cell population size remains unchanged during homeostasis,
346 indicating the differential activity of feedback mechanisms. Moreover, the vastness of the neoblast
347 population in homeostasis allows to examine the ability of neoblasts to respecify their lineage over time,
348 and to determine if FSTF inhibition results in an increase to cell loss rate.
349
350 We examined whether the suppression of a major lineage production has resulted in overproduction of
351 other lineages, a phenomenon that we did not observe in colonies. First, we used two published gene
352 expression datasets from FACS-purified S/G2/M neoblasts in *zfp-1* (RNAi) and control animals collected at
353 various time points (Cheng et al., 2018; van Wolfswinkel et al., 2014) (Methods). We utilized pre-
354 calculated tables of differentially expressed genes in these datasets (Hoffman and Wurtzel, 2023), and
355 annotated the cell types that express them (Fincher et al., 2018). Most downregulated genes with known
356 neoblast lineage enrichment (Fincher et al., 2018) were epidermal (82%, 55/67; Fig 5A; Table S1;
357 Methods). Conversely, upregulated genes following *zfp-1* suppression were primarily associated with
358 protonephridial or neural neoblasts (30/57 and 20/57 genes, respectively; Fig 5B; Table S2), consistent
359 with the original data analysis (Cheng et al., 2018). Notable upregulated genes included transcription
360 factors, such as *nkx2-like* (Currie et al., 2016), *hunchback-like* (Reddien et al., 2005a), *runt-1* (Sandmann
361 et al., 2011; Wenemoser et al., 2012), and *tgs-1* (Zeng et al., 2018). Upregulation was evident from an
362 intermediate time point (9 days post RNAi), whereas epidermal genes downregulation occurred earlier (6
363 days post RNAi; 30%, 20/67; FDR < 1E-5).
364
365 We hypothesized that biologically meaningful upregulation of neuron- and protonephridia-associated
366 genes in neoblasts following *zfp-1* inhibition would result in overexpression of genes associated with these
367 cell types in whole tissues, reflecting their increased production. To test this hypothesis, we examined
368 published gene expression data from whole and regenerated tissues following *zfp-1* inhibition (van

369 Wolfswinkel et al., 2014; Zeng et al., 2018). Predictably, the majority of downregulated genes were
370 associated with the epidermis (70%, 490/698; Fold change < -2; FDR < 1E-5; Table S3; Methods).
371 Examination of upregulated genes showed that only a small fraction of the genes was associated with
372 either protonephridial (4.9%) or neural (12.7%) expression at any examined time point (Fig 5C; Table S4;
373 Methods). Therefore, gene expression analysis of whole tissues provided no evidence of an
374 overrepresentation of neural or protonephridia cells in *zfp-1* (RNAi) animals, suggesting that cells related
375 to these lineages were not excessively produced. Conversely, 37% of the upregulated genes following *zfp-*
376 *1* (RNAi) in the whole tissue libraries were associated with intestinal cell types, despite no evidence for
377 overrepresentation of intestine-associated FSTFs in neoblasts isolated from *zfp-1* (RNAi) animals
378 compared to controls (Table S4).
379
380 In *zfp-1* (RNAi) neoblast colonies, we observed an absolute reduction in cycling cells (Fig 3D). We tested
381 whether this phenotype was recapitulated in homeostatic, unirradiated, *zfp-1* (RNAi) animals by EdU
382 labeling. We injected *zfp-1* or control double-stranded (dsRNA; Methods), and following three and five
383 days, we performed EdU labeling by a 16 hour EdU pulse (Methods). Interestingly, there was an increase
384 in EdU^+ nuclei in the *zfp-1* (RNAi) animals at both time points (Fig 5D). Investigating the potential
385 correlation with apoptosis via TUNEL labeling revealed no early increase in cell death, which only
386 increased at later stages (Fig 5E; Methods). Therefore, *zfp-1* inhibition does not trigger an acute rise in
387 neoblast cell death that might induce hyperproliferation.
388
389 Colony sizes following *zfp-1* (RNAi) were reduced, yet cycling cell numbers in homeostasis were increased.
390 Similar results were reported for the epidermal regulator *Smed-p53* (Cheng et al., 2018; Pearson and
391 Sánchez Alvarado, 2010): neoblast colonies following *Smed-p53* (RNAi) are strikingly smaller (Wagner et
392 al., 2012), yet in homeostasis, *Smed-p53* (RNAi) animals show an increased number of mitoses (Pearson
393 and Sánchez Alvarado, 2010), and even an initial increase in canonical neoblast markers (Pearson and
394 Sánchez Alvarado, 2010).
395

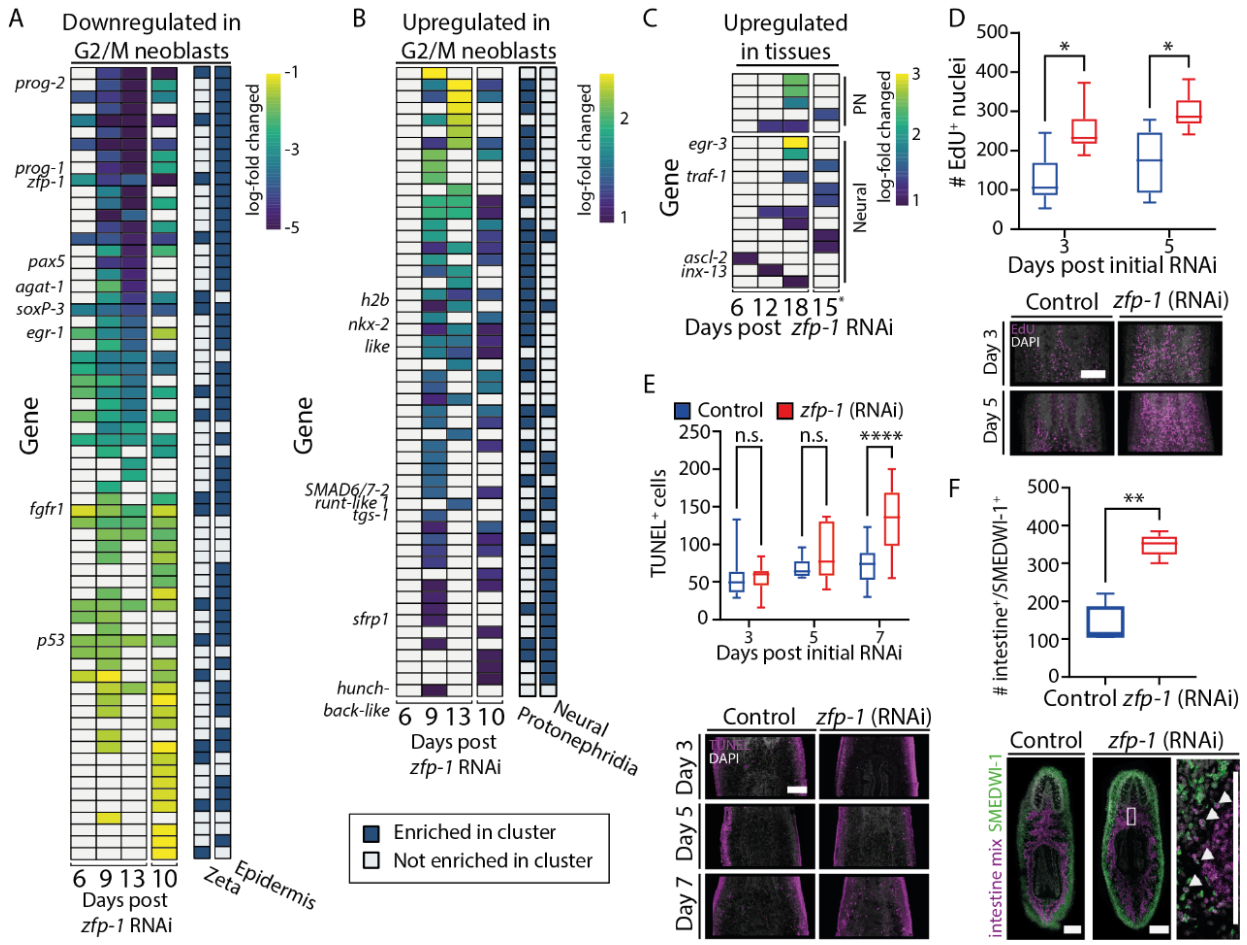

Figure 5. Analysis of *zfp-1* inhibition consequences in homeostasis. (A) Downregulated genes in FACS-purified S/G2/M neoblasts were overwhelmingly associated with expression in the epidermal lineage and epidermis-specialized (zeta) neoblasts (Cheng et al., 2018; Fincher et al., 2018; van Wolfswinkel et al., 2014). (B) Upregulated genes in FACS-purified S/G2/M neoblasts were largely associated with neuronal and protonephridial specialized gene expression (Fincher et al., 2018). (C) Analysis of upregulated genes of whole tissues following *zfp-1* inhibition showed that only a few factors were associated with protonephridia or neurons. (A-C) Heatmaps showing row-scaled gene expression obtained from PLANAtools (Hoffman and Wurtzel, 2023). Blue and yellow, low and high log-fold gene expression difference, respectively. Columns on the right indicate cell type-specific gene expression (Fincher et al., 2018). (D) Counting EdU⁺ nuclei in unirradiated control and *zfp-1* (RNAi) animals. (E) Counting apoptotic cells in unirradiated control and *zfp-1* (RNAi) animals (Methods). (F) Counting intestinal progenitors showed an increase in progenitors at later time points, in agreement with the gene expression analysis of *zfp-1* (RNAi) of whole tissues. Scale = 100 µm. * $P < 0.05$; ** $P < 0.01$; **** $P < 0.0001$.

Considering that in homeostasis *zfp-1* (RNAi) planarians show greater numbers of cycling cells (Fig 5D) and intestinal gene upregulation in tissue (Table S4) as compared with controls, we conducted a targeted analysis to quantify the number of newly generated intestine progenitors in *zfp-1* (RNAi) animals. We

413 counted intestine progenitors *in situ* (Fig 5F; Methods) and found a higher proportion of intestine
414 progenitors in the *zfp-1* (RNAi) animals as compared with controls (Fig 5F; Mann–Whitney two-tailed U
415 test $P = 0.008$). Interestingly, in our analyses of growing colonies, we did not observe a parallel difference
416 in intestine neoblast proportion (Fig 4A), leading us to speculate that the rise in cycling cells in homeostasis
417 was an indirect effect of *zfp-1* suppression, and highlighting the limitations of neoblast analysis in colonies.
418 In other words, integration of the analysis from homeostasis with our colony data suggests that *zfp-1*
419 inhibition did not lead to a direct amplification of other lineages, but more likely to an indirect
420 amplification of the intestine lineage.

421 **Discussion**

422 Understanding how stem cell proliferation and lineage choices are regulated is critical for elucidating
423 mechanisms of growth and homeostasis (Chan et al., 2021; Dagan et al., 2022; Ferraro et al., 2010; Lei et
424 al., 2016; Li and Xie, 2005; Morrison and Spradling, 2008; Scimone et al., 2010; Zhu et al., 2015).
425 Neoblasts form a simple yet powerful system, which has features of both adult stem cells and their transit-
426 amplifying cell progeny (Adler and Sánchez Alvarado, 2015; Baguñà, 2012; Reddien, 2018). Functionally,
427 neoblasts can repopulate stem cell-depleted planarians, produce a diversity of cell types, and adjust their
428 growth rate according to organism requirements and nutrient availability (Hayashi et al., 2006; Salvetti et
429 al., 2009; Steele and Lange, 1976; Wang et al., 2018). Herein, we sought to test whether growth in a
430 neoblast colony is consistent with a model that does not assume communication between neoblasts or
431 memory of cell fate decisions, but instead relies on stochastic selection of division outcome (Fig 6). We
432 further sought to enrich this model by understanding the interplay between neoblast lineage decisions
433 and colony growth.

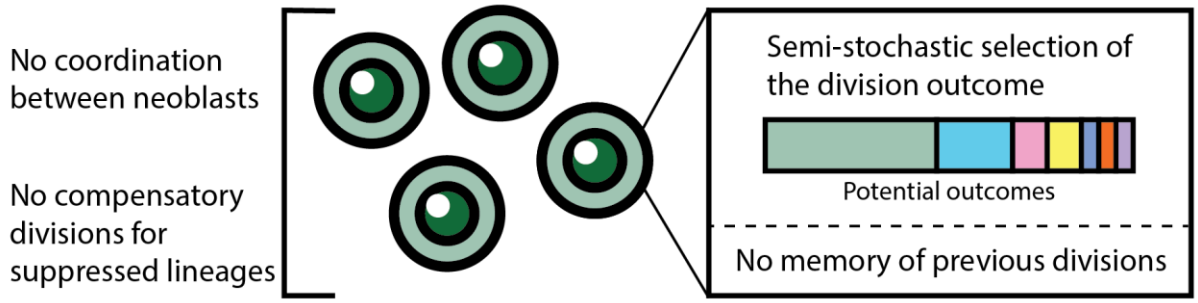

Figure 6. Model summarizing neoblast colony growth principles.

434 **Analysis of neoblast colony expansion**

435 The initial model we developed was grounded in simple principles of colony growth (Eq 1, Fig 2B), in which
436 cell fate decisions are made stochastically and independently of one another, as a function of the following
437 parameters: average cell cycle length, symmetric renewal rate, and symmetric differentiation and
438 neoblast elimination rate. We experimentally derived parameter values and compared the model's
439 predictions to experimental data. Our findings suggested that the reliance on minimal assumptions
440 provides a good description of neoblast colony growth following subtotal irradiation. The model captured
441 the average colony growth within the tested time range, despite notable variability in observed colony
442 sizes at a given time point. Based on these results, we suggest that if slow cycling neoblasts (Molinaro et
443 al., 2021) emerge in colonies, their contribution to colony growth is likely negligible, allowing their
444 exclusion from the model without sacrificing accuracy.
445
446 To better understand the potential consequences of random neoblast loss or excessive symmetric
447 differentiation at early stages of colony growth, we used colony growth simulations, where each cell
448 selected independently the outcome of its division. These simulations predicted that a fraction of colonies
449 would fail to develop because of these random effects, a prediction that was corroborated by
450 experimental results. This alignment demonstrates the utility of neoblasts as a system for studying stem
451 cell colony formation and exploring concepts of stem cell behavior.

452 **Consequences of lineage-specific differentiation inhibition**

453 Moving from the fundamental aspects of neoblast colony growth, we next tested how limiting lineage
454 identity selection affected neoblasts. We suppressed the expression of key fate-specifying genes to dissect
455 how stem cells respond to inhibition of their differentiation trajectory. The transition from measuring
456 general colony growth to specific lineage perturbations allowed us to examine the association of
457 proliferation and lineage specification. In particular, suppressing the master epidermal regulator *zfp-1*,
458 corresponding to the most abundant planarian cell lineage (Cheng et al., 2018; Raz et al., 2021; van
459 Wolfswinkel et al., 2014), drastically reduced neoblast colony growth. Interestingly, suppression of *Smed-*
460 *p53*, a TF expressed in neoblasts and required for epidermal cell production, has resulted in a similar
461 reduction in colony size (Wagner et al., 2012). These findings led us to consider how stem cells in a colony
462 balance self-renewal and differentiation, and why both processes were disrupted by blocking
463 differentiation to a single lineage. We suggest several interpretations for this observation: First, if we

464 assume that a neoblast can alternate between self-renewal and production of differentiated progeny in
465 each cell cycle, then a decision to produce a blocked progeny may preclude further divisions of the
466 neoblast. A second possibility is that the presence of a specific lineage, epidermal progenitors in this case,
467 is required for other neoblasts to proliferate; in this case, suppression of differentiation could indirectly
468 limit colony growth. The first interpretation is more likely relevant for understanding colony growth given
469 our observation that combined suppression of several smaller lineages produced a similar inhibition to
470 colony growth and establishment.

471 The progressive reduction in colony size indicated that inhibition of a specific lineage reduced the fraction
472 of neoblasts that contributed to colony growth, possibly due to their failure to produce the blocked
473 lineage and to alter their progeny identity. Interestingly, in unirradiated animals with abundant neoblasts,
474 *zfp-1* inhibition led to increased cell proliferation – a response also noted after suppressing other
475 regulatory genes like *Smed-p53* (Pearson and Sánchez Alvarado, 2010). This proliferation increase
476 appeared before a rise in cell death, suggesting that cell death did not induce excessive proliferation in
477 early stages. The difference in the consequence of lineage suppression in a neoblast colony and in
478 unirradiated animals indicates that differential activity of feedback mechanisms regulates neoblast
479 proliferation. We speculate that following subtotal irradiation, the near complete depletion of neoblasts
480 and their progeny (Eisenhoffer et al., 2008), alters the regulation of surviving neoblasts, and leading to
481 their rapid proliferation, which is not typical for neoblasts in homeostasis (Wenemoser and Reddien,
482 2010). Further investigation is needed into compensatory mechanisms that planarians use to maintain
483 overall tissue integrity when differentiation processes are disrupted.

484 **A stochastic model for independent selection of cell division outcome in colonies**

485 Our study investigates the mechanism behind neoblast division outcome selection. An exponential growth
486 function describes the increase in colony size and the differentiation of progeny in the timescale of the
487 analysis, closely aligning with our experimental results and published data (Raz et al., 2021; Wagner et al.,
488 2012). Notably, this function operates without parameters for coordination of division outcome between
489 neoblasts or neoblast memory. It posits that division outcomes are guided by an innate distribution of cell
490 fates encoded within the neoblasts. We hypothesize that this distribution is modifiable by regional signals
491 (e.g., Wnt, BMP), which indicate the neoblast location (Gaviño and Reddien, 2011; Petersen and Reddien,
492 2008; Wurtzel et al., 2017), and by injury signals (e.g., ERK), that modulate division rate (Bohr et al., 2021;
493 Fan et al., 2023; Tasaki et al., 2011; Wurtzel et al., 2015). This strategy facilitates the dynamic balance in

494 cell lineage production and meeting the organism's needs without direct communication between
495 neoblasts, and promotes return to homeostasis.
496
497 The emerging model enhances the understanding of neoblast dynamics and contributes to broader
498 knowledge of stem cell behavior. The interplay between lineage-specific differentiation, proliferation, and
499 resultant physiological adaptations presents a robust strategy for using pluripotent stem cells to re-
500 achieve balance, in a manner that is not found in many non-regenerative organisms. This could inspire
501 future research on pluripotent stem cells and their applications in regenerative biology.
502

503 ## Methods

504 ### Gene cloning and transformation

505 Selected genes were amplified using planarian cDNA and gene-specific primers, and cloned into pGEM-T
506 Easy vector using pGEM-T Easy Vector System I (Promega; CAT A1360). Vectors were transformed into
507 *Escherichia coli* using the heat-shock method. Briefly, 5 µL of cloned plasmid were mixed with 100 µL of
508 *E. coli* TOP10 bacteria and incubated on ice for 30 min. Next, bacteria were incubated for 45 s at 42°C,
509 moved immediately to ice, and recovered in 350 µL of Luria Broth (LB) medium for 1 h at 37°C. Then, 100
510 µL of recovered bacteria were plated on agarose plates containing 1:1,000 Ampicillin, 1:200 Isopropyl β-
511 d-1-thiogalactopyranoside (IPTG) and 1:625 5-bromo-4-chloro-3-indolyl-b-D-galactopyranoside (X-Gal).
512 Plates were incubated overnight at 37°C, and colonies were screened by colony PCR using M13F and M13R
513 primers with the following PCR program: (i) 5 min at 95°C; (ii) 34 cycles of 45 s at 95°C, 60 s at 55°C, and 2
514 min at 72°C; (iii) 7 min at 72°C; (iv) hold at 10°C. Reactions were analyzed by gel electrophoresis, and
515 colonies having the correct fragment were grown overnight in LB medium, supplemented with 1:1,000
516 Ampicillin at 37°C at 180 rpm. Plasmids were purified with the NucleoSpin Plasmid MiniprepKit (CAT
517 740588, Macherey-Nagel) and sequenced by Sanger sequencing. Primer sequences used for cloning the
518 following genes: *hnf-4*, forward primer GATCTCGCACAATGCACTCG, reverse primer
519 GTCTCACGAACTCCTTGCCA; *nkx2.2*, forward primer TTTGGTGCCAGCAGACTCAA, reverse primer
520 TAGAGCCAGCTAATGTGGCG; *gata4/5/6*, forward primer CGGTATTGTCGAATTCTCACCAG, reverse primer
521 TGACATCGCAATTGGAACCG; *foxF-1*, forward primer GTCCTATTTCCAGCACACAGC, reverse primer
522 TCCGGAATCGTGCTGAGG.

523 **Near complete neoblast ablation by subtotal irradiation**

524 Animals were irradiated using a BIOBEAM GM 8000 (Gamma-Service Medical GmbH). To generate 1-3
525 colonies per animal, 2 mm starved (> 7 days) worms were irradiated with 1750 rads (Wagner et al., 2012).
526 Worms were allowed to recover and washed in planarian water a day after the irradiation.

527 **Synthesis of dsRNA for feedings and microinjections**

528 DsRNA was synthesized as previously described (Rouhana et al., 2013). Briefly, templates for in vitro
529 transcription (IVT) were prepared by PCR amplification of cloned target genes using forward and reverse
530 primers with flanking T7 promoter sequences on the 5' end. dsRNA was synthesized using the
531 TranscriptAid T7 High Yield Transcription Kit (CAT K0441, Thermo Scientific). Reactions were incubated
532 overnight at 37°C and then supplemented with RNase-free DNase for 30 min. RNA was purified by ethanol
533 precipitation and resuspended in 70 µL of ultra-pure H_2O. RNA was analyzed on 1% agarose gel and
534 quantified by Qubit (CAT Q33223, Thermo Scientific) for validating a concentration higher than 5 µg/µL.
535 Animals were starved for at least 7 days prior to RNAi experiments. In clonal expansion experiments,
536 animals were fed with 14 µL of dsRNA mixed with 25 µL of beef liver 4 days post-irradiation. In
537 homeostasis experiments, worms were injected 4 times with dsRNA every other day.

538 **Injections of dsRNA into planarians**

539 Animals were injected with *zfp-1* dsRNA using Nanoject III (CAT 3-000-207, Drummond Scientific
540 company). Briefly, planarians were placed on a cold wet filter paper on their dorsal side, and were injected
541 posterior to the pharyngeal cavity. After the initial puncture, 3 consecutive dsRNA injections of 33 nL each
542 were delivered at a rate of 66 nL/sec. Worms were injected 4 times, every other day, and fixed at different
543 time points for whole-mount analysis.

544 **Planarian fixation for whole-mount assays**

545 Fixation was performed as previously described (King and Newmark, 2013). Animals were killed with 5%
546 N-Acetyl-L-Cysteine (NAC, CAT 1124220100, Mercury) in PBS for 5 min, then incubated with 4%
547 Formaldehyde (FA) in 0.3% PBSTx (Phosphate Buffered Saline, 0.3% Triton X-100) for 20 min. Animals were
548 then washed in PBSTx, 50:50 PBSTx:methanol and stored in methanol at -20°C.

549 **Fluorescence *in situ* hybridization using tyramide signal amplification**

550 Fluorescence *in situ* hybridization (FISH) was performed as previously described (King and Newmark,
551 2013) with minor changes. Briefly, fixed animals were bleached and treated with proteinase K (2 µg/mL,
552 CAT 25530-049; Invitrogen) in PBSTx (Phosphate Buffered Saline, 0.3% Triton X-100). Samples were
553 incubated for 2 hr in a pre-hybridization buffer (pre-hyb) followed by an overnight incubation with probes.
554 Samples were washed twice for 30 min in each solution: pre-hyb solution, 1:1 pre-hyb:2×SSCx, 2×SSCx,
555 0.2×SSCx, PBSTx. Blocking was performed in 0.5% Roche Western Blocking Reagent (CAT 11921673001;
556 Sigma-Aldrich) and 5% heat-inactivated horse serum (CAT 04-124-1A; Biological Industries) in TNTx
557 (100 mM Tris pH 7.5, 150 mM NaCl, 0.3% Triton X-100) for 2 hr. Animals were incubated with an anti-DIG-
558 POD antibody (1:1,500; Roche) or anti-DNP-HRP (1:10,000; Perkin-Elmer) overnight at 4°C. After antibody
559 washes, tyramide development was performed as previously described (King and Newmark, 2018).
560 Following development, peroxidase activation was quenched in a 1% sodium azide solution for 1 hr,
561 followed by 6 PBSTx washes and antibody labeling for the second probe. Samples were labeled with DAPI
562 (1:5000 in PBSTx) overnight at 4°C and mounted with Vectashield (CAT H-1000-10; Vector Laboratories).

563 **Immunofluorescence combined with FISH**

564 Animals were fixed with 5% NAC, bleached, and treated with proteinase K as described for FISH analysis.
565 Samples were incubated for 2 hr in pre-hyb followed by overnight incubation with the probes. Samples
566 were washed twice in each solution, for 30 min each: pre-hyb solution, 1:1 pre-hyb:2×SSCx, 2×SSCx,
567 0.2×SSCx, PBSTx. Subsequently, blocking was performed in PBSTB (PBSTx, 0.25% BSA) for 2 hr at room
568 temperature. Animals were then incubated with anti-SMEDWI-1 antibody (a gift from Peter W. Reddien,
569 1:1000) at 4°C overnight. Then, 7 PBSTx washes were performed, followed by incubation with PBSTB
570 blocking solution for 2 hr at room temperature followed by incubation with secondary antibody (goat anti
571 rabbit-HRP, 1:300 in PBSTB) overnight at 4°C. Post-antibody washes and tyramide development
572 (fluorescein tyramide; 1:2000) were performed as previously described (King and Newmark, 2013). After
573 development, peroxidase activity was quenched using 1% sodium azide for 1 hr, followed by 6 PBSTx
574 washes and incubation with anti-DIG antibody (1:1,500; CAT 11207733910; Sigma-Aldrich) overnight at
575 4°C. Post-antibody washes and development with rhodamine tyramide (1:1000) were performed as
576 described above. Samples were incubated with DAPI (1:5000 in PBSTx) overnight and mounted with
577 Vectashield.

578 **FISH by hybridization chain reaction**

579 Probe sets (30 pairs per gene) were designed and synthesized by the manufacturer (Molecular
580 Instruments, Los Angeles, CA, USA) for the following genes: *tgs-1* and *smedwi-1*. Worms were fixed and
581 bleached as previously described for FISH. Next, hybridization chain reaction (HCR) was performed
582 according to the manufacturer's HCR RNA-FISH protocol for samples in solution (Choi et al., 2018). DAPI
583 was added during the amplifier's wash steps, for a total incubation time of 2 hr at room temperature.
584 Samples were mounted with Vectashield and stored at 4°C for subsequent analysis.

585 **Metabolic labeling by F-ara-EdU**

586 F-ara-EdU (CAT T511293; Sigma-Aldrich) was first diluted in DMSO to the concentration of 200 mg/mL.
587 Animals were soaked with 2.5 mg/mL F-ara-EdU diluted in planarian water for 16 hr, 24 hr after the
588 indicated injections. For clonal expansion analysis, samples were soaked with EdU for 16 hr at day 11 post
589 irradiation. Samples were fixed, bleached, and treated with proteinase K as described for FISH (King and
590 Newmark, 2013). Next, 3 washes in 3% PBSB (PBS supplemented with 3% BSA) were performed followed
591 by a click reaction using baseclick kit (CAT Back-edu488, baseclick GmbH). Samples were washed 3 times
592 with PBSB, incubated with DAPI (1:5,000 in PBSTx) overnight at 4°C and mounted with Vectashield.

593 **Immunofluorescence labeling by anti-H3P labeling**

594 H3P labeling was performed as previously described (LoCascio et al., 2017; Wenemoser and Reddien,
595 2010) with minor modifications. Briefly, following fixation with 5% NAC, bleaching and proteinase K
596 treatment, blocking was performed with 10% heat inactivated horse serum for 2 hr. Next, anti-phospho-
597 Histone H3 Antibody (CAT 04817; Sigma-Aldrich) was added in the concentration of 1:100 overnight at
598 4°C, followed by 7 PBSTx washes. Samples were incubated in blocking solution for 2 hr and then incubated
599 with goat anti-rabbit-HRP secondary antibody (Abcam; ab6721; 1:300) overnight at 4°C. Samples were
600 washed 7 times with PBSTx, developed using rhodamine tyramide diluted 1:1,000 in PBSTi (PBSTx, 0.07%
601 imidazole), labeled with DAPI overnight at 4°C, and mounted with Vectashield.

602 **Image acquisition and cell counting**

603 Images of samples labeled by FISH, HCR, immunofluorescence, F-ara-EdU and TUNEL were collected using
604 a Zeiss LSM800 confocal microscope. Labeled cells were counted manually using the cell counter module
605 in the ImageJ software (Rueden et al., 2017). Normalization of EdU^+ nuclei was performed by dividing the

606 number of EdU$^+$ nuclei by the average number of *smedwi-1*$^+$ cells detected in a colony at the corresponding
607 time point, and divided by 10 for readability.

608 **TUNEL labeling**

609 TUNEL was performed as previously described (Pellettieri, 2010) with minor modifications. Briefly,
610 animals were fixed with 5% NAC and bleached overnight with 6% hydrogen peroxide in PBSTx. Animals
611 were then treated with 2 µg/mL proteinase K for 10 min, 4% FA for 10 min, and were then washed twice
612 with PBS. Using ApopTag Red *In Situ* Apoptosis Detection Kit (CAT S7165; Sigma-Aldrich), 5 animals per
613 tube were incubated with TdT enzyme mix for 4 hr at 37°C, followed by 4 PBSTx washes. Samples were
614 incubated in a blocking solution (0.5% Roche Western Blocking Reagent and 5% inactivated horse serum
615 in TNTx) for 2 hr followed by incubation with anti-DIG antibody (1:1000) overnight at 4°C. Samples were
616 washed 7 times with PBSTx, developed using rhodamine tyramide diluted 1:1,000, labeled with DAPI
617 (1:5000 in PBSTx) overnight at 4°C and mounted with Vectashield.

618 **Assumptions underlying neoblast colony growth model**

619 The model assumes that stem cell colony growth dynamics are governed by three key parameters:
620 symmetric renewal probability, elimination probability, and cell cycle duration. Cell cycle duration
621 represents the average time required for a single cell division. The model assumes universal probabilities
622 for stem cells in the colony, and does not incorporate environmental, niche, or intercellular effects.
623 Additionally, no memory of previous cell divisions is assumed. While Raz et al. reported the potential of
624 minor memory effects in neoblast divisions, these have been determined to have a negligible impact on
625 the colony (Raz et al., 2021) and, therefore, on the model predictions. Symmetric renewal and elimination
626 probabilities remain constant throughout the simulation, and fate specification is guided by predefined
627 fate distributions derived from prior studies (Raz et al., 2021; Scimone et al., 2018, 2014b; van
628 Wolfswinkel et al., 2014).

629 **Estimation of the fraction of symmetric renewal divisions**

630 Estimation of the fraction of symmetric renewal divisions was performed as previously described (Lei et
631 al., 2016; Raz et al., 2021). Colonies at 7 dpi were labeled by FISH with the pan-neoblast marker *smedwi-*
632 *1.* Colonies were closely examined using a confocal microscope (Zeiss LSM800) to find two adjacent
633 *smedwi-1*$^+$ cells. Two spatially distinct labeled cells with high expression of *smedwi-1* marker were

634 classified as symmetric division. Pairs composed of high *smedwi-1*$^+$ cell and low *smedwi-1*$^+$ cell were
635 classified as asymmetrically dividing.

636 **Data extraction from published literature**

637 Data was extracted using WebPlotDigitizer by labeling data points (Drevon et al., 2017). Table S5
638 summarizes the extracted data and the original data source.

639 **Estimation of values of colony growth parameters**

640 Counts of neoblast in colonies at different time points following subtotal irradiation (Fig 2F, Table S5) were
641 collected. Curve fitting using an exponential function (Eq 2) was performed with the curve_fit function
642 from the scipy.optimize Python module using the average cell cycle length (τ) extracted from the BrdU$^+$
643 labeling assay (Fig 2C; S1B-E) (Lei et al., 2016). The values of symmetric renewal (p) and symmetric
644 differentiation or elimination (q) were estimated by fitting a range of values for $p - q$ between 0.1 and 0.4
645 and calculating the R-squared values of the fit to the data (S1D-E). Experimental assessment of symmetric
646 renewal (p) and asymmetric division (a) determined that they were equal (i.e., $p = a$; Fig 2D). The best fit
647 for $p - q$, as estimated by examining the sum square of residuals (Fig S1B-E), was found to be 0.345. Since
648 (1) all possible division outcomes are $p + q + a = 1$; (2) $p = a$; and (3) $p - q = 0.345$, we estimated that $p =$
649 0.45 and $q = 0.1$.

650 **Simulation of colony growth**

651 Simulations were performed using custom R code, executing as follows: selection of parameters occurred
652 using selected frequencies of symmetric renewal and symmetric differentiation or elimination. Initial
653 colony size was determined by randomly selecting a value from empirical distribution of early colony size,
654 as reported in the literature (Raz et al., 2021; Wagner et al., 2011). In each simulation round, every cell
655 underwent selection of an outcome, adhering to the predefined frequencies. This simulation process
656 extended 5 – 20 cycles and was replicated 100 times.

657 **Gene expression analysis of S/G2/M neoblasts**

658 Processed differential gene expression data profiling FACS-purified S/G2/M neoblasts isolated from
659 control and *zfp-1* (RNAi) animals was downloaded from PLANATools (Hoffman and Wurtzel, 2023). Each
660 gene in the table was assigned a cell type identity based on the planarian cell type gene expression atlas
661 (Fincher et al., 2018).

662 **Statistical analyses**

663 Statistical tests were performed using GraphPad Prism (v 10.0.3), using the scipy stat module (v 1.12), and
664 R (v 4.3.2). Statistical significance was assessed using Mann-Whitney two-tailed U test or two-tailed
665 Student's t-test and threshold for considering an effect significant was 0.05, unless stated otherwise.
666

667 **Supplementary Figures**

668 **Figure S1**

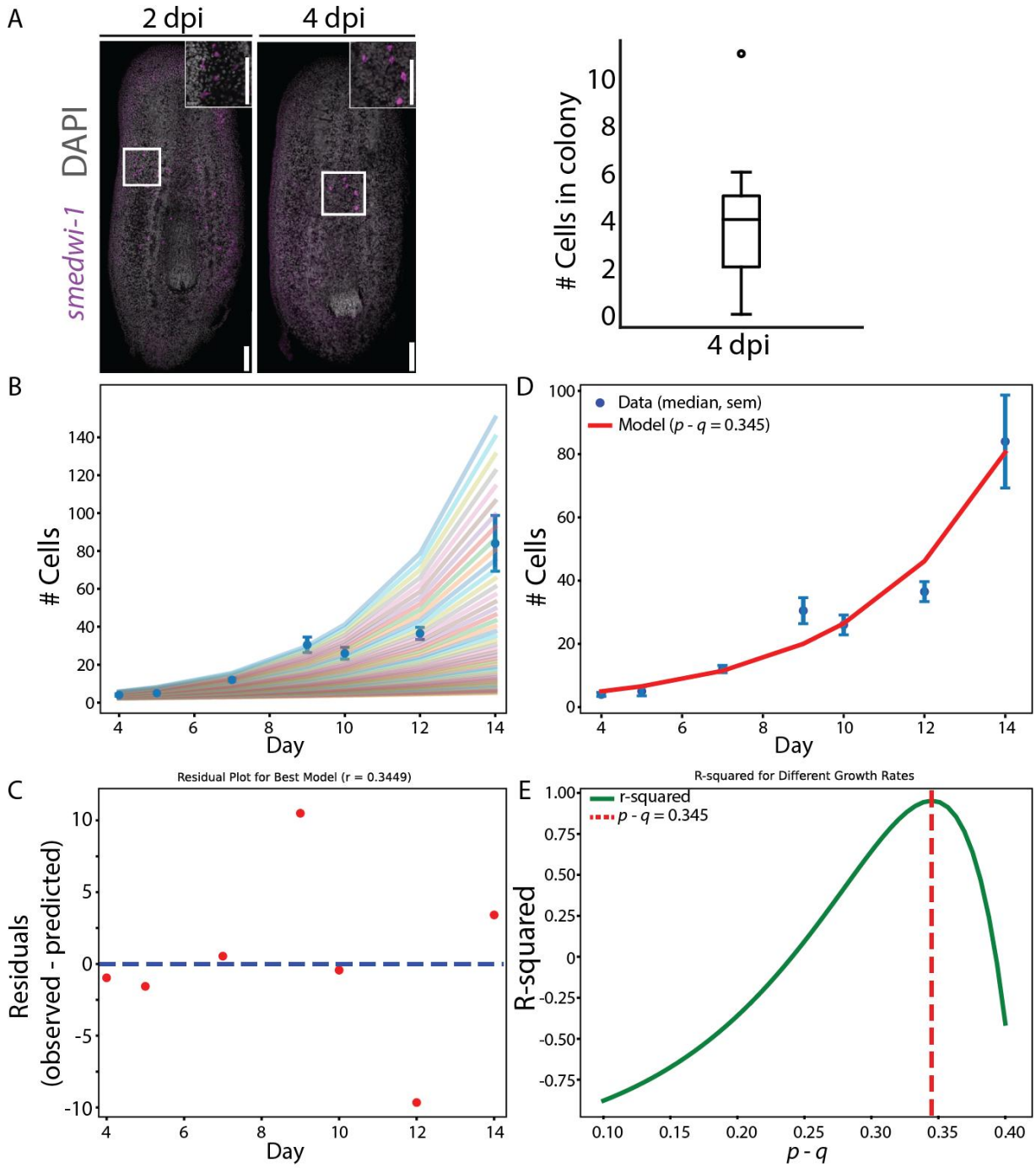

669

670 **Figure S1. Analysis of colony growth. (A) Shown are FISH images for detecting neoblasts (*smedwi-1*⁺; magenta) at 2 and 4 days**
671 **post irradiation (dpi), left and right, respectively. Colonies were not found at 2 dpi, and instead, isolated cells expressing low**
672 **levels of *smedwi-1* were scattered in the planarian parenchyma, likely reflecting remnants of dying neoblasts. At 4 dpi,**

673 **surviving neoblasts already established spatially-isolated cluster of neoblasts detectable as small colonies (median = 4 cells;**
674 **quantification shown on the right). (B-E) The effect of different growth parameters on colony size. (B) Shown are colony sizes**
675 **when considering a range of *q* values (0.1 - 0.4) with the experimentally determined *p* = 0.5. Data collected here and in**
676 **published analyses of colony sizes (Raz et al., 2021; Wagner et al., 2012) is shown as median (blue dots, and standard error of**
677 **the mean). (C) Shown is the best predicted fit growth following colony establishment using the exponential growth equation.**
678 **(D) Analysis of residuals between observed and predicted colony sizes using the best fitting parameters. (E) Shown is the r-**
679 **squared difference between observed and predicted data at a range of growth parameters. The minimal r-squared value is**
680 **indicated by the red dashed line.**
681

682 **Figure S2**

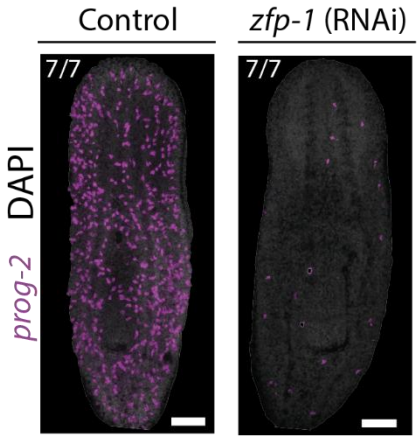

683

684 **Figure S2. Inhibition of epidermal progenitors by a single *zfp-1* dsRNA injection. Inhibition of *zfp-1* resulted in complete ablation**
685 **of epidermal progenitor production at 7 days post injection, as observed by labeling animals with the epidermal progenitor**
686 **marker, *prog-2*.**

687

688 **Figure S3**

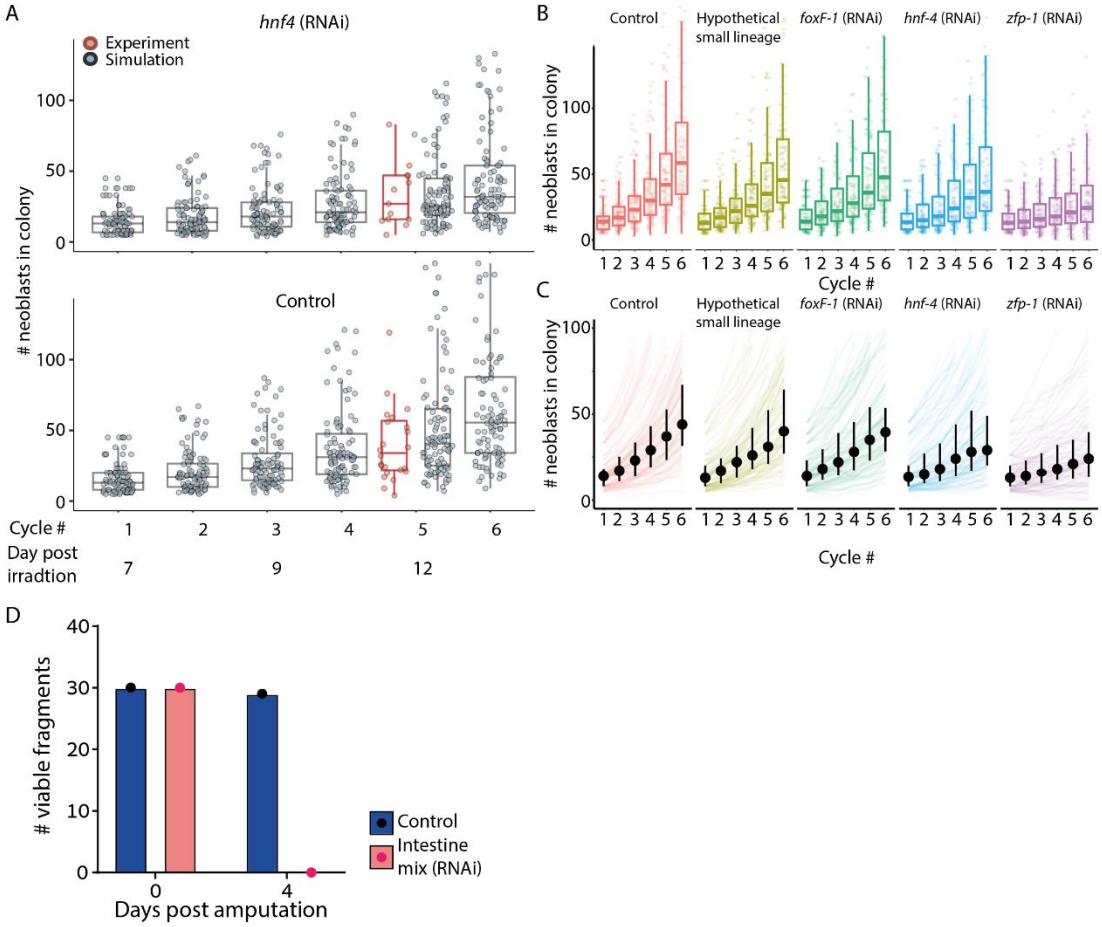

689

690 **Figure S3. Simulation of colony size following RNAi. (A) Simulation (gray) and comparison to experimental data (red) of**
691 **neoblast colonies in control and *hnf-4* (RNAi) animals. The simulation indicates that given the variability in colony size,**
692 **detecting significant differences in colony size is unlikely for this lineage. Each dot represents a single simulation (gray) or an**
693 **experimentally determined size (red). (B-C) Simulations of colony sizes over 6 cycles of replication starting approximately at**
694 **day seven post irradiation. (B) Boxplots showing the distribution of colony sizes (horizontal line, median; box, interquartile**
695 **range (IQR); vertical line, 99% range). Each dot represents a single simulation. (C) Simulation of colony growth (line) shows**
696 **growth over time (dot, median; vertical line, IQR). (D) The RNAi efficacy was evaluated through assessment of viability of**
697 **fragments obtained from animals following a single feeding of dsRNA that targeted intestine FSTFs (*hnf-4, gata4/5/6, nkx2.2*),**
698 **compared to a non-targeting control dsRNA (*unc22*). All fragments derived from worms fed with dsRNA targeting intestine**
699 **FSTFs died within four days post-feeding, demonstrating that a single dsRNA feeding induced a robust effect.**

700 ## Supplementary Tables

701 **Table S1**

702 Table S1. Downregulated genes in G2/M neoblasts following *zfp-1* (RNAi)

703 **Table S2**

704 Table S2. Upregulated genes in G2/M neoblasts following *zfp-1* (RNAi)

705 **Table S3**

706 Table S3. Downregulated genes in tissues or blastema following *zfp-1* (RNAi)

707 **Table S4**

708 Table S4. Upregulated genes in tissues or blastema following *zfp-1* (RNAi)

709 **Table S5**

710 Table S5. Summary of data extraction using WebPlotDigitizer

711 ## Author contributions

712 T.F. and O.W. designed the project. T.F. performed all experiments with support from P.V.C, Y.Y., and
713 S.D.. T.F. performed microscopy and imaging analysis. O.W. performed simulations and RNAseq data
714 analysis. T.F. and O.W. wrote and edited the manuscript.

715 ## Declaration of Interests

716 The authors declare no competing interests.

717 ## Acknowledgments

718 We thank Prof. David Sprinzak, Prof. Iftach Nachman, and Dr. Yasmine Meroz for their critical input. We
719 thank Shrey Jain for his assistance with performing FISH. We thank members of the Wurtzel lab for
720 feedback and discussions. We thank Dr. Daria Makarovsky from the interdepartmental services at Tel Aviv
721 University's Faculty of Medicine for assistance with gamma irradiation. O.W. is supported by the Israel

722 Science Foundation (grant 2039/18) and the European Research Council (no. 853640). O.W. is a
723 Zuckerman Faculty Scholar.
724

References

Abkowitz JL, Golinelli D, Harrison DE, Guttorp P. 2000. In vivo kinetics of murine hemopoietic stem cells. *Blood* **96**:3399–3405. doi:10.1182/blood.V96.10.3399

Adler CE, Sánchez Alvarado A. 2015. Types or states? cellular dynamics and regenerative potential. *Trends Cell Biol* **25**:687–696. doi:10.1016/j.tcb.2015.07.008

Baguñà J. 2012. The planarian neoblast: the rambling history of its origin and some current black boxes. *Int J Dev Biol* **56**:19–37. doi:10.1387/ijdb.113463jb

Becker KA, Ghule PN, Therrien JA, Lian JB, Stein JL, van Wijnen AJ, Stein GS. 2006. Self-renewal of human embryonic stem cells is supported by a shortened G1 cell cycle phase. *J Cell Physiol* **209**:883–893. doi:10.1002/jcp.20776

Bohr TE, Shiroor DA, Adler CE. 2021. Planarian stem cells sense the identity of the missing pharynx to launch its targeted regeneration. *eLife* **10**. doi:10.7554/eLife.68830

Chan A, Ma S, Pearson BJ, Chan D. 2021. Collagen IV differentially regulates planarian stem cell potency and lineage progression. *Proc Natl Acad Sci USA* **118**. doi:10.1073/pnas.2021251118

Cheng L-C, Tu KC, Seidel CW, Robb SMC, Guo F, Sánchez Alvarado A. 2018. Cellular, ultrastructural and molecular analyses of epidermal cell development in the planarian *Schmidtea mediterranea*. *Dev Biol* **433**:357–373. doi:10.1016/j.ydbio.2017.08.030

Choi HMT, Schwarzkopf M, Fornace ME, Acharya A, Artavanis G, Stegmaier J, Cunha A, Pierce NA. 2018. Third-generation in situ hybridization chain reaction: multiplexed, quantitative, sensitive, versatile, robust. *Development* **145**. doi:10.1242/dev.165753

Currie KW, Molinaro AM, Pearson BJ. 2016. Neuronal sources of *hedgehog* modulate neurogenesis in the adult planarian brain. *eLife* **5**. doi:10.7554/eLife.19735

Dagan Y, Yesharim Y, Bonneau AR, Frankovits T, Schwartz S, Reddien PW, Wurtzel O. 2022. m6A is required for resolving progenitor identity during planarian stem cell differentiation. *EMBO J* **41**:e109895. doi:10.15252/embj.2021109895

Drevon D, Fursa SR, Malcolm AL. 2017. Intercoder reliability and validity of webplotdigitizer in extracting graphed data. *Behav Modif* **41**:323–339. doi:10.1177/0145445516673998

Eisenhoffer GT, Kang H, Sánchez Alvarado A. 2008. Molecular analysis of stem cells and their descendants during cell turnover and regeneration in the planarian *Schmidtea mediterranea*. *Cell Stem Cell* **3**:327–339. doi:10.1016/j.stem.2008.07.002

Fan Y, Chai C, Li P, Zou X, Ferrell JE, Wang B. 2023. Ultrafast distant wound response is essential for whole-body regeneration. *Cell* **186**:3606-3618.e16. doi:10.1016/j.cell.2023.06.019

Ferraro F, Celso CL, Scadden D. 2010. Adult stem cells and their niches. *Adv Exp Med Biol* **695**:155–168. doi:10.1007/978-1-4419-7037-4_11

759 Fincher CT, Wurtzel O, de Hoog T, Kravarik KM, Reddien PW. 2018. Cell type transcriptome atlas for the
760 planarian *Schmidtea mediterranea*. *Science* **360**. doi:10.1126/science.aaq1736

761 Forsthoefel DJ, James NP, Escobar DJ, Stary JM, Vieira AP, Waters FA, Newmark PA. 2012. An RNAi
762 screen reveals intestinal regulators of branching morphogenesis, differentiation, and stem cell
763 proliferation in planarians. *Dev Cell* **23**:691–704. doi:10.1016/j.devcel.2012.09.008

764 Gaviño MA, Reddien PW. 2011. A Bmp/Admp regulatory circuit controls maintenance and regeneration
765 of dorsal-ventral polarity in planarians. *Curr Biol* **21**:294–299. doi:10.1016/j.cub.2011.01.017

766 González-Estévez C, Felix DA, Rodríguez-Esteban G, Aboobaker AA. 2012. Decreased neoblast progeny
767 and increased cell death during starvation-induced planarian degrowth. *Int J Dev Biol* **56**:83–91.
768 doi:10.1387/ijdb.113452cg

769 Hayashi T, Asami M, Higuchi S, Shibata N, Agata K. 2006. Isolation of planarian X-ray-sensitive stem cells
770 by fluorescence-activated cell sorting. *Dev Growth Differ* **48**:371–380. doi:10.1111/j.1440-
771 169X.2006.00876.x

772 Hoffman M, Wurtzel O. 2023. PLANAtools-An interactive gene expression repository for the planarian
773 *Schmidtea mediterranea*. *Front Cell Dev Biol* **11**:1149537. doi:10.3389/fcell.2023.1149537

774 King RS, Newmark PA. 2018. Whole-Mount In Situ Hybridization of Planarians. *Methods Mol Biol*
775 **1774**:379–392. doi:10.1007/978-1-4939-7802-1_12

776 King RS, Newmark PA. 2013. In situ hybridization protocol for enhanced detection of gene expression in
777 the planarian *Schmidtea mediterranea*. *BMC Dev Biol* **13**:8. doi:10.1186/1471-213X-13-8

778 Lei K, Thi-Kim Vu H, Mohan RD, McKinney SA, Seidel CW, Alexander R, Gotting K, Workman JL, Sánchez
779 Alvarado A. 2016. *Egf* signaling directs neoblast repopulation by regulating asymmetric cell division in
780 planarians. *Dev Cell* **38**:413–429. doi:10.1016/j.devcel.2016.07.012

781 Levin M, Pietak AM, Bischof J. 2019. Planarian regeneration as a model of anatomical homeostasis:
782 Recent progress in biophysical and computational approaches. *Semin Cell Dev Biol* **87**:125–144.
783 doi:10.1016/j.semcdb.2018.04.003

784 Li L, Xie T. 2005. Stem cell niche: structure and function. *Annu Rev Cell Dev Biol* **21**:605–631.
785 doi:10.1146/annurev.cellbio.21.012704.131525

786 LoCascio SA, Lapan SW, Reddien PW. 2017. Eye Absence Does Not Regulate Planarian Stem Cells during
787 Eye Regeneration. *Dev Cell* **40**:381-391.e3. doi:10.1016/j.devcel.2017.02.002

788 Mangel M, Bonsall MB, Aboobaker A. 2016. Feedback control in planarian stem cell systems. *BMC Syst*
789 *Biol* **10**:17. doi:10.1186/s12918-016-0261-8

790 Molinaro AM, Lindsay-Mosher N, Pearson BJ. 2021. Identification of TOR-responsive slow-cycling
791 neoblasts in planarians. *EMBO Rep* **22**:e50292. doi:10.15252/embr.202050292

792 Morrison SJ, Spradling AC. 2008. Stem cells and niches: mechanisms that promote stem cell
793 maintenance throughout life. *Cell* **132**:598–611. doi:10.1016/j.cell.2008.01.038

794 Passegué E, Jamieson CHM, Ailles LE, Weissman IL. 2003. Normal and leukemic hematopoiesis: are
795 leukemias a stem cell disorder or a reacquisition of stem cell characteristics? *Proc Natl Acad Sci USA*
796 **100 Suppl 1**:11842–11849. doi:10.1073/pnas.2034201100

797 Pearson BJ, Sánchez Alvarado A. 2010. A planarian p53 homolog regulates proliferation and self-renewal
798 in adult stem cell lineages. *Development* **137**:213–221. doi:10.1242/dev.044297

799 Pearson BJ. 2022. Finding the potency in planarians. *Commun Biol* **5**:970. doi:10.1038/s42003-022-
800 03905-9

801 Pellettieri J. 2010. Cell death and tissue remodeling in planarian regeneration. *Dev Biol*.

802 Petersen CP, Reddien PW. 2008. *Smed-betacatenin-1* is required for anteroposterior blastema polarity in
803 planarian regeneration. *Science* **319**:327–330. doi:10.1126/science.1149943

804 Raz AA, Wurtzel O, Reddien PW. 2021. Planarian stem cells specify fate yet retain potency during the cell
805 cycle. *Cell Stem Cell* **28**:1307-1322.e5. doi:10.1016/j.stem.2021.03.021

806 Reddien PW, Bermange AL, Murfitt KJ, Jennings JR, Sánchez Alvarado A. 2005a. Identification of genes
807 needed for regeneration, stem cell function, and tissue homeostasis by systematic gene perturbation
808 in planaria. *Dev Cell* **8**:635–649. doi:10.1016/j.devcel.2005.02.014

809 Reddien PW, Oviedo NJ, Jennings JR, Jenkin JC, Sánchez Alvarado A. 2005b. SMEDWI-2 is a PIWI-like
810 protein that regulates planarian stem cells. *Science* **310**:1327–1330. doi:10.1126/science.1116110

811 Reddien PW. 2018. The cellular and molecular basis for planarian regeneration. *Cell* **175**:327–345.
812 doi:10.1016/j.cell.2018.09.021

813 Reddien PW. 2013. Specialized progenitors and regeneration. *Development* **140**:951–957.
814 doi:10.1242/dev.080499

815 Rouhana L, Weiss JA, Forsthoefel DJ, Lee H, King RS, Inoue T, Shibata N, Agata K, Newmark PA. 2013.
816 RNA interference by feeding in vitro-synthesized double-stranded RNA to planarians: methodology
817 and dynamics. *Dev Dyn* **242**:718–730. doi:10.1002/dvdy.23950

818 Rueden CT, Schindelin J, Hiner MC, DeZonia BE, Walter AE, Arena ET, Eliceiri KW. 2017. ImageJ2: ImageJ
819 for the next generation of scientific image data. *BMC Bioinformatics* **18**:529. doi:10.1186/s12859-017-
820 1934-z

821 Salvetti A, Rossi L, Bonuccelli L, Lena A, Pugliesi C, Rainaldi G, Evangelista M, Gremigni V. 2009. Adult
822 stem cell plasticity: neoblast repopulation in non-lethally irradiated planarians. *Dev Biol* **328**:305–314.
823 doi:10.1016/j.ydbio.2009.01.029

824 Sandmann T, Vogg MC, Owlarn S, Boutros M, Bartscherer K. 2011. The head-regeneration transcriptome
825 of the planarian *Schmidtea mediterranea*. *Genome Biol* **12**:R76. doi:10.1186/gb-2011-12-8-r76

826 Scimone ML, Kravarik KM, Lapan SW, Reddien PW. 2014a. Neoblast specialization in regeneration of the
827 planarian *Schmidtea mediterranea*. *Stem Cell Reports* **3**:339–352. doi:10.1016/j.stemcr.2014.06.001

828 Scimone ML, Lapan SW, Reddien PW. 2014b. A forkhead transcription factor is wound-induced at the
829 planarian midline and required for anterior pole regeneration. *PLoS Genet* **10**:e1003999.
830 doi:10.1371/journal.pgen.1003999

831 Scimone ML, Meisel J, Reddien PW. 2010. The Mi-2-like *Smed-CHD4* gene is required for stem cell
832 differentiation in the planarian Schmidtea mediterranea. *Development* **137**:1231–1241.
833 doi:10.1242/dev.042051

834 Scimone ML, Wurtzel O, Malecek K, Fincher CT, Oderberg IM, Kravarik KM, Reddien PW. 2018. *foxF-1*
835 Controls Specification of Non-body Wall Muscle and Phagocytic Cells in Planarians. *Curr Biol* **28**:3787-
836 3801.e6. doi:10.1016/j.cub.2018.10.030

837 Singh SR, Burnicka-Turek O, Chauhan C, Hou SX. 2011. Spermatogonial stem cells, infertility and
838 testicular cancer. *J Cell Mol Med* **15**:468–483. doi:10.1111/j.1582-4934.2010.01242.x

839 Steele VE, Lange CS. 1976. Effects of irradiation on stem cell response to differentiation inhibitors in the
840 planarian *Dugesia etrusca*. *Radiat Res* **67**:21–29.

841 Tasaki J, Shibata N, Nishimura O, Itomi K, Tabata Y, Son F, Suzuki N, Araki R, Abe M, Agata K, Umesono Y.
842 2011. ERK signaling controls blastema cell differentiation during planarian regeneration. *Development*
843 **138**:2417–2427. doi:10.1242/dev.060764

844 Tu KC, Cheng L-C, T K Vu H, Lange JJ, McKinney SA, Seidel CW, Sánchez Alvarado A. 2015. *Egr-5* is a post-
845 mitotic regulator of planarian epidermal differentiation. *eLife* **4**:e10501. doi:10.7554/eLife.10501

846 Van Roten A, Barakat AZA-Z, Wouters A, Tran TA, Mouton S, Noben J-P, Gentile L, Smeets K. 2018. A
847 carcinogenic trigger to study the function of tumor suppressor genes in *Schmidtea mediterranea*. *Dis*
848 *Model Mech* **11**. doi:10.1242/dmm.032573

849 van Wolfswinkel JC, Wagner DE, Reddien PW. 2014. Single-cell analysis reveals functionally distinct
850 classes within the planarian stem cell compartment. *Cell Stem Cell* **15**:326–339.
851 doi:10.1016/j.stem.2014.06.007

852 Wagner DE, Ho JJ, Reddien PW. 2012. Genetic regulators of a pluripotent adult stem cell system in
853 planarians identified by RNAi and clonal analysis. *Cell Stem Cell* **10**:299–311.
854 doi:10.1016/j.stem.2012.01.016

855 Wagner DE, Wang IE, Reddien PW. 2011. Clonogenic neoblasts are pluripotent adult stem cells that
856 underlie planarian regeneration. *Science* **332**:811–816. doi:10.1126/science.1203983

857 Wang IE, Wagner DE, Reddien PW. 2018. Clonal Analysis of Planarian Stem Cells by Subtotal Irradiation
858 and Single-Cell Transplantation. *Methods Mol Biol* **1774**:479–495. doi:10.1007/978-1-4939-7802-1_20

859 Wenemoser D, Lapan SW, Wilkinson AW, Bell GW, Reddien PW. 2012. A molecular wound response
860 program associated with regeneration initiation in planarians. *Genes Dev* **26**:988–1002.
861 doi:10.1101/gad.187377.112

862 Wenemoser D, Reddien PW. 2010. Planarian regeneration involves distinct stem cell responses to
863 wounds and tissue absence. *Dev Biol* **344**:979–991. doi:10.1016/j.ydbio.2010.06.017

Wurtzel O, Cote LE, Poirier A, Satija R, Regev A, Reddien PW. 2015. A Generic and Cell-Type-Specific Wound Response Precedes Regeneration in Planarians. *Dev Cell* **35**:632–645. doi:10.1016/j.devcel.2015.11.004

Wurtzel O, Oderberg IM, Reddien PW. 2017. Planarian Epidermal Stem Cells Respond to Positional Cues to Promote Cell-Type Diversity. *Dev Cell* **40**:491-504.e5. doi:10.1016/j.devcel.2017.02.008

Zeng A, Li H, Guo L, Gao X, McKinney S, Wang Y, Yu Z, Park J, Semerad C, Ross E, Cheng L-C, Davies E, Lei K, Wang W, Perera A, Hall K, Peak A, Box A, Sánchez Alvarado A. 2018. Prospectively isolated Tetraspanin+ neoblasts are adult pluripotent stem cells underlying planaria regeneration. *Cell* **173**:1593-1608.e20. doi:10.1016/j.cell.2018.05.006

Zhu SJ, Hallows SE, Currie KW, Xu C, Pearson BJ. 2015. A *mex3* homolog is required for differentiation during planarian stem cell lineage development. *eLife* **4**. doi:10.7554/eLife.07025